

Read our COVID-19 research and news.



RESEARCH ARTICLE | HEALTH AND MEDICINE

Vascular disrupting agent induced aggregation of gold nanoparticles for photothermally enhanced tumor vascular disruption

 Sheng Hong, Di-Wei Zheng, Cheng Zhang, Qian-Xiao Huang, Si-Xue Cheng and  Xian-Zheng Zhang*

+ See all authors and affiliations

Science Advances 05 Jun 2020:
Vol. 6, no. 23, eabb0020
DOI: 10.1126/sciadv.abb0020

Article

Figures & Data

Info & Metrics

eLetters

PDF

Help

Abstract

Although vascular disrupting agents (VDAs) have been extensively implemented in current clinical tumor therapy, the notable adverse events caused by long-term dosing severely limit the therapeutic efficacy. To improve this therapy, we report a strategy for VDA-induced aggregation of gold nanoparticles to further destroy tumor vascular by photothermal effect. This strategy could effectively disrupt tumor vascular and cut off the nutrition supply after just one treatment. In the murine tumor model, this strategy results in notable tumor growth inhibition and gives rise to a 92.7% suppression of tumor growth. Besides, enhanced vascular damage could also prevent cancer cells from distant metastasis. Moreover, compared with clinical therapies, this

INTRODUCTION

Tumor angiogenesis is one of the typical characteristics for solid tumors (1–3). During tumor growth, the vasculature not only provides O₂ and nutrients but also clears CO₂ and metabolic wastes produced in tumor tissue (4). Moreover, the tumor vasculature also provides a transport pathway for tumor distant metastasis. Playing an important role in tumor growth, proliferation, and metastasis, tumor vessels have been recognized as a promising target for tumor treatment (5, 6). Consequently, tumor vascular disrupting agents (VDAs), as representative vascular targeting therapeutic agents, have been successfully developed for the treatment of a variety of tumor types (7). As one of the typical small-molecule VDAs in current clinical trial, DMXAA (5,6-dimethylxanthenone-4-acetic acid ASA404) could selectively target the tumor vascular endothelium, destroy the tumor vasculature, and cut off the tumor blood supply, leading to the ischemic necrosis of tumor cells (8, 9). It is reported that DMXAA has been widely studied in current clinical tumor therapy and has achieved some success in different tumor types (8, 9).

Although DMXAA can inhibit tumor growth and metastasis to some extent, the single dose, is unable to inhibit tumor growth for a long time, and long-term dosing is required. Thus, side effects caused by frequent dosing, including urinary incontinence, anxiety, visual impairment, and thrombosis, always appear (10, 11). Statistically, up to 83.9% of treated patients suffer from the varying degree of side effects. As a result, these adverse effects lead to a decreased quality of life and reduced treatment adherence of patients during therapy, causing difficulty maintaining continuous therapy and markedly decreasing the effectiveness of treatment (12).

In consideration of the remarkable limitations in current vascular disrupting therapy, we attempt to improve this therapy by combining it with photothermal therapy (PTT), an emerging therapy with spatiotemporal controllability and high efficiency (13–16). Hyperthermia can lead to injury of vascular endothelial cells in tumor tissues and decrease the repair ability of vascular, which may act as a complementary therapy for the vascular disrupting therapy. As a promising photothermal therapeutic agent, gold nanoparticles (AuNPs) have been intensively investigated for PTT (17–19). The photothermal conversion efficiency of AuNPs is closely related to the particle size. Only the large particles are equipped with high photothermal conversion efficiency for PTT (20). However, compared with the small AuNPs, the large ones exhibit shorter blood residence time and longer biological half-life, which are typically undesirable in biomedical applications (21). Therefore, controllably assembling small AuNPs into large aggregates may be a good strategy to solve the contradictory problem (22, 23). To our knowledge, DMXAA could selectively target the tumor vessels and activate the coagulation cascade, resulting in the assembling of soluble fibrinogen into insoluble gel-like fibrin within tumor vessels (9). Inspired by this special assembling behavior, we expect that

enhanced tumor vascular disruption (peTVVD). Thus, the administration of DMXAA will lead to the disruption of tumor vessels and the activation of coagulation cascade. Once coagulation cascade is activated, the fAuNPs will assemble into insoluble clots in tumor vessels due to the fibrinogen aggregation. Afterward, near-infrared irradiation is performed for further photothermal ablation of tumor vascular and the combination of VDAs with PTT for enhanced tumor vascular disruption (**Fig. 1**). To improve current vascular disrupting therapy, we developed a strategy for DMXAA-induced AuNPs aggregation in tumor vessels to combine VDA with PTT for combined tumor vascular disruption. The peTVD strategy would cause not only the tumor growth suppression through nutrient exchange blockage but also the tumor metastasis inhibition by cutting off the metastatic process. We expect that this peTVD strategy could effectively enhance tumor vascular damage, reduce dosing frequency, and avoid the side effects caused by frequent administration.

[Download high-res image](#) | [Open in new tab](#) | [Download Powerpoint](#)

Fig. 1 The schematic diagram of peTVD strategy.

The administration of DMXAA leads to the disruption of tumor vessels, which will induce the aggregation of AuNPs in tumor vessels. Afterward, near-infrared irradiation is performed for further photothermal ablation of tumor vascular, achieving the combination of VDAs with PTT for peTVD. Fb, fibrinogen.

RESULTS

In vitro aggregation behavior of fAuNPs

In response to bleeding, the prothrombin in plasma is activated to thrombin followed by converting soluble fibrinogen into insoluble fibrin clots (**24**). First, the aggregation of fAuNPs with the treatment of thrombin was studied in vitro (**Fig. 2A**). The morphology change of the nanoparticles was observed with transmission electron microscope (TEM). It was observed that the monodispersed fAuNPs could be assembled into aggregates with the addition of thrombin (**Fig. 2B** and fig. S1). The stability of fAuNPs was tested, which was found to exhibit high dispersity in various mediums, including deionized water, phosphate-buffered saline (PBS), and serum (fig. S2). To further characterize the aggregation of fAuNPs in solution, the hydrodynamic sizes before and after aggregation were measured with dynamic light scattering. The average hydrodynamic sizes of as-prepared AuNPs and fAuNPs were around 43.8 and 78.8 nm, respectively (**Fig. 2C**), and the increased size of fAuNPs was attributed to the fibrinogen molecules conjugation on the particles.

PDF

Help

2D, the monodispersed AuNPs and fAuNPs showed a characteristic absorption peak at around 530 nm, while another absorption peak appeared at near-infrared (NIR) region after the addition of thrombin, indicating the formation of aggregates. In addition, the increased A_{650}/A_{530} values after the addition of thrombin also manifested the aggregation of fAuNPs (**Fig. 2E**, where A_{650} is the absorption value at 650 nm and A_{530} is that at 530 nm).

[Download high-res image](#) | [Open in new tab](#) | [Download Powerpoint](#)

Fig. 2 The aggregation of fAuNPs in vitro.

(A) Schematic representation of thrombin-induced aggregation of fAuNPs. (B) TEM images of solutions containing fAuNPs in the absence (left) and presence (right) of thrombin. (C) Hydrodynamic sizes of AuNPs, fAuNPs, and aAuNPs in the absence and presence of thrombin. a.u., arbitrary units. UV-vis absorption spectra (D) and the corresponding absorption values (E) of AuNPs, fAuNPs, and aAuNPs in the absence and presence of thrombin. Photothermal images (F) and corresponding photothermal conversion curves (G) of PBS, fAuNPs, and aAuNPs upon laser irradiation (808 nm, 1 W cm^{-2}).

The strong absorption peak in NIR region thus gives aggregated AuNPs (aAuNPs) enough photothermal conversion ability, which is potentially applied in PTT (**25, 26**). After confirming the aggregation behavior of fAuNPs, the photothermal conversion ability of aAuNPs was further studied. According to **Fig. 2 (F and G)**, the temperature of the aqueous solution containing aAuNPs increased by 22.1°C under the 808-nm laser irradiation (1 W cm^{-2} , 8 min), while the temperature of the AuNPs solution and PBS only increased by 4.2° and 2.2°C , respectively. These results indicate that fAuNPs could be assembled into aggregates under coagulation mechanism, which would have the potential to be applied in PTT.

In vivo tumor targeting and aggregation of fAuNPs

After investigating the in vitro aggregation of fAuNPs, the in vivo targeting and aggregation were further studied. Currently, as a small-molecule VDA in clinical trial, DMXAA selectively targets and disrupts tumor vessels, leading to a hemorrhage within tumors. As shown in **fig. S3A**, tumors treated with DMXAA displayed more hemorrhage sites compared to the control, demonstrating the disruption of tumor vessels by DMXAA. In general, hemorrhage would lead to subsequent platelets activation and coagulation cascade accompanied by the conversion of fibrinogen into fibrin in hemorrhage sites for hemostasis. To confirm whether fibrinogen could target to the hemorrhage

observed in **PBS**-treated tumors (fig. S3B). These results confirmed that DMXAA could specifically induce hemorrhage in tumors and further direct the fibrinogen to the hemorrhage sites.

Then, the targeting of fAuNPs to tumor region through selectively induced coagulation cascade by DMXAA was studied. The tumor targeting of fAuNPs was firstly studied by in vivo fluorescence imaging system. As displayed in **Fig. 3A**, after the DMXAA injection, the fluorescence intensity in tumor increased gradually within 12 hours, which suggested a rapid accumulation of fAuNPs in tumors. In contrast, no obvious change of the fluorescence intensity was observed in tumors without the treatment of DMXAA, and the intratumoral fAuNPs contents at 12 and 24 hours after DMXAA injection were, respectively, 2.6- and 2.1-fold higher than that of control groups (**Fig. 3B**), indicating that DMXAA treatment could effectively direct the fAuNPs into tumors. Images from three-dimensional (3D) reconstructed transillumination fluorescent imaging also showed that the treatment of DMXAA was efficient in inducing tumor-specific accumulation of fAuNPs (**Fig. 3C**). To further confirm the in vivo tumor-targeted efficiency of fAuNPs under DMXAA treatment, the content of Au in tumor tissues and major organs (spleen, liver, kidney, lung, and heart) was determined by using inductively coupled plasma mass spectrometry (ICP-MS). As shown in **Fig. 3D**, all the groups had high levels of Au contents in the liver, spleen, lung (reticuloendothelial system), and kidney. As for the tumors, DMXAA-treated group showed apparently higher Au content at 12 and 24 hours than that of the control group. In general, AuNPs have the high elemental atomic number and efficient x-ray absorption property, which provide superior contrast for the computed tomography (CT) imaging (**27**). Micro-CT imaging was performed to measure the AuNPs content in tumor tissues for further evaluating the in vivo tumor-targeting efficiency. Images in **Fig. 3 (E and F)** revealed that enhanced micro-CT signal in tumor after treatment with DMXAA, further demonstrating the tumor-specific accumulation of fAuNPs with DMXAA treatment.

PDF

Help

[Download high-res image](#) | [Open in new tab](#) | [Download Powerpoint](#)

Fig. 3 Tumor targeting and aggregation of fAuNPs in vivo.

(A) In vivo fluorescence images of CT26 tumor-bearing mice following administration of fAuNPs or fAuNPs + DMXAA at different time points. The in vivo fluorescence of Cy5 was used to determine the accumulation of fAuNPs. (B) Corresponding relative fluorescence intensity at tumor sites after administration of fAuNPs or fAuNPs + DMXAA. For quantitative comparison, the regions of interest were drawn over tumor. (C) 3D reconstructed transillumination fluorescent imaging for revealing the accumulation of fAuNPs in tumors with DMXAA treatment. (D) Biodistribution of fAuNPs at 12 and 24 hours after injection of fAuNPs with or without DMXAA treatment. (E) Micro-CT images of CT26 tumor bearing mice at 0 and 12 hours after injection of fAuNPs with or without DMXAA

SD. The results are representative of three independent experiments. Significance between each group was calculated using analysis of variance (ANOVA) with Tukey's post hoc test. * $P < 0.05$, ** $P < 0.01$, and *** $P < 0.001$.

After investigating the tumor targeting of fAuNPs with DMXAA treatment, whether the coagulation cascade could also lead to the aggregation of fAuNPs in tumor as well was further studied. The aggregation of fAuNPs would result in strong absorption in NIR region, which could give aAuNPs high photoacoustic signal and photothermal conversion capability. The photoacoustic imaging was performed to confirm the aggregation of fAuNPs in tumor. It was observed that the tumor treated with DMXAA showed an obvious photoacoustic signal at 12 hours after injection, while a negligible photoacoustic signal was observed in tumor treated with PBS (**Fig. 3G**). Meanwhile, the photothermal imaging was also performed to confirm the aggregation of fAuNPs in tumor. As displayed in **Fig. 3 (H and I)**, the tumor local temperature in DMXAA-treated group was raised by 26.7°C after 10 min of irradiation with 808-nm laser (1 W cm^{-2}), while the temperature of control tumor was only raised by 5.6°C . These results indicated that the administration of DMXAA was efficient in inducing tumor-specific accumulation and aggregation of fAuNPs in vivo, thus making it possible to achieve the combination of DMXAA with PTT for peTVD.

Tumor vascular disruption

Next, the ability of peTVD strategy to effectively disrupt the tumor vascular was assessed. CD31, a typical vascular endothelial cell marker, was staining on tumor sections to visualize the tumor vessels. CT26 tumor-bearing mice were treated with peTVD or control formulations through intravenous injection, and the intratumoral microvessel density (MVD) of tumors was measured 24 hours. Confocal images in **Fig. 4A** and fig. S4 show that tumor sections from control group exhibited strong CD31 fluorescence, demonstrating the high MVD of tumors, while a much weaker of CD31 fluorescence signal was observed in peTVD-treated tumors compared with DMXAA- or **PBS**-treated groups. It was observed from **Fig. 4B** that the peTVD-treated tumors exhibited a 63.5% decreased intratumoral MVD, confirming a fine vascular disruption ability of peTVD treatment.

[Download high-res image](#) | [Open in new tab](#) | [Download Powerpoint](#)

Fig. 4 Tumor vascular disruption.

(green) in a percent per CD31⁺ area (red) on eight fields from three tumors per group. Scale bars, 100 μm . Inset scale bars, 20 μm . **(G)** Representative tumor images and the Evans blue content in different group treated with Evans blue. CT26 tumor-bearing mice with different treatments were injected intravenously with Evans blue (5%). The tumors were harvested and photographed after 3 hours (inset). Then, the tumors were soaked in formamide for 3 days to extract the Evans blue. The Evans blue were quantified by measuring the absorption at 620 nm with UV-vis spectrophotometer. Micro-CT images **(H)** and quantification **(I)** of tumor vessels in different group ($n = 3$) visualized by CT angiography. The CT signal was estimated by calculating the gray values of tumors. Data are shown as the means \pm SD. The results are representative of three independent experiments. Significance between each group was calculated using ANOVA with Tukey's post hoc test. * $P < 0.05$, ** $P < 0.01$, and *** $P < 0.001$.

Vascular collapse would lead to the increased vessel permeability, reduced vascular perfusion, and declined blood flow (28). Next, the permeability of tumor vessels was investigated through surveying the vascular leakage by FITC-labeled dextran (29). FITC-labeled dextran was intravenously injected at 24 hours after treatment of peTVD, and the tumors were harvested 30 min later. Compared with the control group, tumor sections in peTVD-treated mice exhibited a 3.5-fold increase in dextran leakage (Fig. 4, C and D). Even when compared with the DMXAA-treated mice, tumor vessels in peTVD-treated mice still showed a 2.0-fold increase in dextran leakage, manifesting a further disruption of tumor vessels on basic of DMXAA (Fig. 4, C and D). To further evaluate the vascular disruption ability of peTVD, the perfusion of tumor vessels was evaluated through intravenous injection of FITC-labeled lectin (29). Consistent with above results, peTVD treatment effectively decreased the tumor vascular perfusion in comparison with PBS and DMXAA, which were found to be decreased by 78.3 and 58.9%, respectively (Fig. 4, E and F). Evans blue, a macromolecular dye for blood volume determination, was also used to investigate the perfusion of tumor vascular (31). Evans blue was intravenously injected into the mice at 24 hours after treatment of mice with peTVD, and subsequently, the tumors were harvested 3 hours later. As shown in Fig. 4G, when compared with control, the peTVD treatment led to a 55.3% decrease permeability and retention for Evans blue in solid tumors, indicating a significant decrease in tumor vascular permeability. To further assess vascular disruption ability of peTVD, the 3D structure of vessels was visualized by CT angiography. After 24-hour treatment of mice with peTVD, tumors were perfused with CT contrast agents, and the vessels were observed by micro-CT imaging. It was observed that the angiography agents in control group spread throughout the tumor vessels, manifesting the intact vasculature of tumors treated with PBS, while peTVD-treated tumor showed discontinuous distribution of contrast agents and weaker CT signal in tumors, indicating that the tumor vasculature was destroyed by peTVD treatment (Fig. 4, H and I). Together, those findings suggested that tumor vessels in peTVD-

disruption might lead to dysfunction of substance exchange and further result in abnormal tumor metabolism. Here, metabolomic analysis on the CT26 tumor models was conducted to evaluate changes in tumor metabolism with peTVD treatment. The abundance of metabolites in tumors treated with peTVD or PBS was identified by gas chromatography–mass spectrometry (GC-MS) analysis (32). As shown in Fig. 5A, 69 kinds of metabolite were identified, and these metabolites could be classified into two unsupervised horizontal clusters by cluster analysis. The principal components analysis (PCA) was also used to analyze the metabolite content in peTVD-treated tumors, which was found to be highly different from that of control groups (Fig. 5B). Besides, the fold change of the metabolite contents in tumors with peTVD treatment against tumors with PBS treatment was calculated, and most of the metabolites (61 of 69) decreased after peTVD treatment (Fig. 5C), which may owe to the nutrition supply deficiency caused by vascular disruption.

[Download high-res image](#) | [Open in new tab](#) | [Download Powerpoint](#)

Fig. 5 Metabolomic analysis.

(A) Heat map representation and cluster analysis of 69 kinds of metabolites in CT26 tumors after treatment with PBS and peTVD. (B) PCA of the metabolites with obvious differences between the PBS and peTVD groups. (C) Fold change (FC) of the metabolite content after treatment with peTVD. $\text{Log}_2(\text{FC}) > 0$ (black) represent the increase of metabolite content $\text{Log}_2(\text{FC}) < 0$ (blue) represent the decrease of metabolite content. (D) Bubble diagram of differential metabolites enriched in various Reactome pathways. Bubble diameters represent the number of metabolites in each pathway. Bubbles were pseudocoloured to show the number of metabolites in each pathway. (E) Heat map of significantly enriched pathways in “metabolism” after treatment with PBS and peTVD. TCA, tricarboxylic acid. (F) Reaction network diagram of metabolism process annotated in the Reactome database. (G) Reaction network diagram of “transport of small molecular” process annotated in the Reactome database. The changed pathways were highlighted in blue, while unchanged pathways were colored with gray. (H) Heat map of significantly enriched pathways in transport of small molecular after treatment with PBS and peTVD. Three biological replicates are shown. HDL, high density lipoprotein.

Furthermore, Reactome database, an open source for analyzing biological responses and pathways, was applied to evaluate the metabolic changes with peTVD treatment (32). Among these biological responses and pathways, the metabolism pathway and transport of small molecules exhibited low false discovery rate values and high enrichment (Fig. 5D and fig. S5). According to table S1, 30.0% of reactions (found: 665; total: 2218) in the network of metabolism pathways were changed after peTVD treatment. Meanwhile, 39.4% of reactions (found: 172; total: 437) in the

These results demonstrated that tumor vessel disruption by peTVD could suppress tumor metabolism by limiting the activity of metabolic processes. What is more, the changes in the affiliated pathway of transport of small molecules were also studied by Reactome database analysis (**Fig. 5G**). Obvious changes in 16 identified pathways were listed in a heat map, and most of them (14 of 16 pathways) were inhibited (**Fig. 5H**). From this analysis, the peTVD strategy was found to inhibit the tumor metabolism in a global perspective.

In vivo therapeutic effect

The in vivo therapeutic effect of peTVD was further investigated on CT26 tumor-bearing mice. Female BALB/c mice were xenografted with CT26 tumor by subcutaneous injection of CT26 tumor cells on their right flank. When the tumor volumes reached to $\sim 100 \text{ mm}^3$, the mice were randomly divided into five groups and treated, respectively, with PBS, fAuNPs with NIR, DMXAA, fAuNPs + DMXAA, and fAuNPs + DMXAA with NIR (peTVD) through tail vein injection. The tumor volume of mice in each group was measured every 2 days. As shown in **Fig. 6A**, obvious inhibition of tumor growth with 92.6% tumor suppression was observed in peTVD-treated group, exhibiting an outstanding therapeutic efficacy compared with other groups. Besides, the tumor weight and tumor images on the 20th day also indicated the extraordinary therapeutic effect of peTVD (**Fig. 6, B and C**). Next, hematoxylin and eosin (H&E) staining and immunofluorescence staining of Ki-67 were used to assess the in vivo therapeutic effect. peTVD-treated group showed an obviously increased necrosis and notably decreased Ki-67 fluorescence intensity (**Fig. 6D**), indicating the inhibition of tumor proliferation after treatment. The weights of mice in all five groups showed no obvious change during the treatment, and the section of major organs (heart, liver, spleen, lung, kidney) stained with H&E did not exhibit abnormality, demonstrating negligible systemic toxicity of those treatments (**Fig. 6E** and fig. S6). The survival of mice with various treatments was further assessed. As shown in **Fig. 6F**, 75% of the mice in peTVD-treated group were still alive at the 60th day, while PBS-treated mice only survived for 33 days. This phenomenon could likely be attributed to the tumor growth suppression of peTVD. The antimetastasis ability of peTVD was evaluated by H&E staining. No obvious metastasis was found in peTVD-treated group, while all other groups showed metastasis in the lung to some extent (**Fig. 6G**), confirming good antimetastasis ability of peTVD. peTVD exhibited efficient tumor suppression and metastases inhibition ability, which may be an effective strategy for tumor treatment.

staining of tumors from mice with different treatments. Scale bars, 200 μm . (E) Body weights of mice with different treatments. Body weight was measured every 2 days up to 20 days. Six biological replicates are shown. (F) The survival curve of mice with different treatments. Eight biological replicates are shown. (G) H&E staining images of lungs from mice with different treatments. The arrows indicate the metastasis. A representative image of three biological replicates is shown. Data are shown as the means \pm SD. Significance between each group was calculated using ANOVA with Tukey's post hoc test. $**P < 0.01$ and $***P < 0.001$.

Subsequently, the comprehensive safety of the peTVD strategy was evaluated both in vitro and in vivo. According to the in vitro hemolysis assay in fig. S7A, after addition into the plasma, neither DMXAA nor fAuNPs caused hemolysis, indicating high blood compatibility of the peTVD strategy. The platelet aggregation assay was also performed to further prove the blood compatibility of this peTVD strategy, As shown in fig. S7B, DMXAA and fAuNPs did not induce observable platelet aggregation, demonstrating that peTVD had no risk of thrombosis. This result was also found in blood coagulation tests [including activated partial thromboplastin time (APTT), prothrombin time (PT), fibrinogen-FIB, and thrombin time (TT)]. After treatment with peTVD, no significant changes were observed in blood coagulation parameters compared to the control group (fig. S8 and table S2). In addition, the blood biochemistry test and blood routine examination were further studied to confirm the safety of the peTVD strategy, and no significant difference in blood parameters after treatment with peTVD could be detected (fig. S9 and table S3), further manifesting good blood compatibility of peTVD strategy.

Comparison of peTVD with clinical therapies

Surgical resection, radiotherapy, and chemotherapy are the three most common therapies for clinical tumor treatment (33). Here, the therapeutic effect was compared between peTVD and clinical therapies. Female BALB/c mice were xenografted with CT26 tumor by subcutaneous injection of luciferase-expressed CT26 cells (luc-CT26) on their right flank. When the tumor volumes reached to $\sim 100 \text{ mm}^3$, the mice were randomly divided into five groups (five mice per group) and treated with PBS, surgical resection, chemotherapy, radiotherapy, and peTVD, respectively. The tumor growth was monitored with the bioluminescence imaging every 7 days. As shown in Fig. 7 (A to C), the chemotherapy and radiotherapy could inhibit tumor growth to a certain extent, and the surgical resection eliminated almost all the tumor tissue at early stage, but tumor recurrence appeared eventually. Compared with those clinical therapies, peTVD treatment could effectively suppress tumor growth with a 95.2% of suppression, and this result may be related to the significant increase in animal survival. As shown in Fig. 7D, mice treated with surgical resection,

Fig. 7 Comparison of peTVD strategy with clinical therapies.

Bioluminescence images (A) and relative bioluminescence intensity (B) of subcutaneous luc-CT26 tumor-bearing mice after treatment with peTVD and clinical therapies. Bioluminescence imaging was performed every 7 days. Five biological replicates are shown. Blank boxes indicate dying mice. (C) The tumor inhibition rates of mice after treatment with peTVD and clinical therapies. (D) The survival curve of mice with different treatments. Eight biological replicates are shown. (E) Representative bioluminescence images of mice after treatment with peTVD and clinical therapies. (F) H&E staining of lungs from mice after treatment with peTVD and clinical therapies. The arrowheads indicate the metastasis. A representative image of three biological replicates is shown. Data are shown as the means \pm SD. Significance between each group was calculated using ANOVA with Tukey's post hoc test. $**P < 0.01$ and $***P < 0.001$.

The antimetastasis abilities of peTVD strategy and these clinical therapies were also compared by bioluminescence imaging. According to the images in Fig. 7E, surgical resection, radiotherapy, and chemotherapy treatment all caused lung metastasis to some degree, while peTVD treatment apparently reduced metastasis, confirming its good antimetastasis ability. Consistent with these findings, the antimetastasis ability assayed by H&E staining also exhibited the same result (Fig. 7F). Those results indicated that peTVD strategy could more effectively suppress tumor growth and inhibit tumor metastases as compared with the clinical therapies, and peTVD strategy may be a promising therapy for tumor treatment in the future.

DISCUSSION

In this study, an enhanced tumor vascular disruption strategy was developed through the combination of VDAs with PTT. Activated by DMXAA, the coagulation-mediated fibrinogen aggregation resulted in fAuNPs assembly to form large aggregates to further destroy tumor vascular by photothermal effect. As a result, this strategy could effectively disrupt the tumor vascular and cut off the nutrition supply of the tumor. The therapeutic efficacy of peTVD strategy was evaluated in mice tumor models, which was found to have potential in tumor therapy. Coincidentally, the tumor vascular disruption by peTVD could also prevent the spread of tumor cells from entering the circulatory system. Furthermore, compared with clinical therapies, peTVD displayed better antitumor effect and antimetastasis ability. This combination therapy could effectively enhance the tumor vascular disruption, which may be helpful in reducing the dosing frequency and the dose-dependent side effects of vascular targeting therapy.

PDF

Help

large number of clinical cases. Thus, the positive biological effect and safety of these drugs made it promising for the clinical application. Besides, the PTT is superior in spatiotemporal controllability and high efficiency, which could selectively destroy the tumor tissues. Hyperthermia can also lead to the tumor vascular damage, acting as a great complementary therapy for the vascular disrupting therapy. In comparison with the preexisting vascular disrupting therapy, our approach displayed a better antitumor effect and antimetastasis ability in murine models with just one dose. It is expected that our approach could effectively reduce the dose-dependent side effects of drugs and might be a promising therapy for tumor treatment.

However, this study still has some limitations. First, owing to the limitation of tissue penetration capacity of light, PTT cannot influence the deep tissue of organism so that our strategy is not applicable for the internal tumors. Besides, the long-term toxicity and metabolism of materials are needed to be well studied. Furthermore, the detailed dose optimization is still required before this strategy can be further tested in large animal models.

In conclusion, this study described a polymerization reaction-mediated AuNPs assembly, which could be induced by coagulation cascade initiated with VDAs. In this study, with the combination of DMXAA, the AuNPs assembly was successfully induced to further disrupt the tumor vascular by PTT in murine tumor models, achieving the tumor growth and metastasis inhibition. Although this improved therapy still exists in the initial stage, we believe that it may have potential in offering previously unidentified sights to improve the current cancer therapies.

MATERIALS AND METHODS

Study design

The objective of this study was to improve the current tumor vascular disrupting therapy for reducing the side effects caused by frequent dosing. We found that functional mechanism of DMXAA could guide the aggregation of AuNPs, which could achieve a further tumor vascular damage through photothermal effect. We attempted to combine the DMXAA-directed vascular damage with photothermal ablation of vascular for enhanced tumor vascular disruption to reduce dosing frequency. Mice treated with this improved vascular disrupting therapy exhibited superior tumor vascular damage than DMXAA alone. Through metabolomic analysis, we found that this therapy could inhibit the tumor metabolism in a global perspective through just one dose, which exhibited efficient tumor suppression and metastases inhibition ability. Compared with clinical therapies, this improved strategy also showed preferable inhibition of tumor growth and metastasis, which may be a promising therapy for tumor treatment in the future.

PDF

Help

otherwise mentioned, female BALB/c mice were xenografted with CT26 tumor by subcutaneous injection of CT26 cells on their right flank.

Preparation of AuNPs and fAuNPs

To prepare AuNPs, trisodium citrate (5 mg) was added rapidly to the HAuCl₄ solution (0.01%, 50 ml) followed by heating under reflux for 8 min. The prepared AuNPs were stored in 4°C for later use.

The fAuNPs was prepared by mixing the as-prepared AuNPs with fibrinogen in tris-HCl buffer (20 mM, pH 7.4) for 30 min. The fibrinogen molecules readily conjugated to AuNPs through electrostatic and hydrophobic interactions. The unreacted fibrinogen molecules were removed by centrifugation at 15,000g for 20 min. The fAuNPs were stored in 4°C for later use.

Fluorescence labeling

FITC-fibrinogen was prepared by directly reacting between FITC and fibrinogen. In brief, the fibrinogen (5 mg ml⁻¹) was mixed with FITC (1%) in PBS and reacted at room temperature for 4 hours. The unbound FITC was removed by dialysis for several times.

The labeling of fAuNPs was conducted with Cy5-*N*-hydroxysuccinimide (NHS) in PBS buffer at pH 7.4. Ten milligrams of fAuNPs was suspended in 5 ml of PBS buffer. Cy5-NHS (1%) were added to the fAuNPs solution and stirred for 4 hours. The products were then collected and purified with ultrafiltration membranes (molecular weight cutoff of 10 kDa) to remove unbound dyes.

The targeting of FITC-fibrinogen with DMXAA treatment

Female BALB/c mice with CT26 tumors (1 × 10⁶ CT26 cells per mouse) inoculated on their right flank were used. When the tumor volume reached to ~100 mm³, the mice were intravenously injected with PBS or DMXAA (15 mg kg⁻¹) followed by injection of FITC-fibrinogen (2 mg ml⁻¹, 100 μl). After 4 hours, the mice in different groups (three mice per group) were sacrificed, and tumors were collected. Subsequently, these tumors were submitted to frozen section and were stained with DAPI (cell nucleus, blue) and anti-CD31 (vessel, red). Images were obtained on a fluorescent microscope.

In vivo fluorescence imaging

Female BALB/c mice with CT26 tumors (1 × 10⁶ CT26 cells per mouse) inoculated on their right flank were used for in vivo fluorescence imaging. When the tumor volume reached to ~100 mm³, the mice were intravenously injected with PBS or DMXAA (15 mg kg⁻¹) followed by injection of fAuNPs

flank were used for in vivo biodistribution. When the tumor volume reached to $\sim 100 \text{ mm}^3$, PBS or DMXAA (15 mg kg^{-1}) was intravenously injected into the mice followed by injection of fAuNPs (1 mg ml^{-1} , $100 \mu\text{l}$). Then, mice in different groups (three mice per group) were sacrificed at 6 and 12 hours after injection of fAuNPs. Tumors and other main organs (liver, spleen, lung, kidney, heart, and brain) were harvested, weighed, and stored at -80°C . All the tissues were lysed in chloroazotic acid, and the Au contents were evaluated by ICP-MS analysis.

In vivo photoacoustic and photothermal imaging

Female BALB/c mice with CT26 tumors (1×10^6 CT26 cells per mouse) inoculated on their right flank were used for photoacoustic and photothermal imaging. When the tumor volume reached to $\sim 100 \text{ mm}^3$, PBS or DMXAA (15 mg kg^{-1}) was intravenously injected into the mice followed by injection of fAuNPs (1 mg ml^{-1} , $100 \mu\text{l}$). Photoacoustic images were performed on a photoacoustic imaging system. Photothermal images were recorded by using a FLIR Ax5 camera under irradiation with an 808-nm laser (1 W cm^{-2}).

In vivo vascular leakage and perfusion assay

Female BALB/c mice with CT26 tumors (1×10^6 CT26 cells per mouse) inoculated on their right flank were used for the vascular leakage and perfusion assay. The mice were randomly divided into three groups (three mice per group). When the tumor volume reached to $\sim 100 \text{ mm}^3$, the mice were treated with PBS, DMXAA (15 mg kg^{-1}), or peTVD. The vascular leakage was studied by intravenous injection of FITC-dextran (70 kDa, 25 mg ml^{-1} , $100 \mu\text{l}$). Thirty minutes after the injection, mice were sacrificed and tumors were collected. The tumor sections were stained with anti-CD31 antibody for the blood vessels (red) and DAPI for the cell nucleus (blue). Intratumoral leakage was estimated by calculating dextran⁺ area (green) in a percent per total area. peTVD treatment, namely, DMXAA (15 mg kg^{-1}), was intravenously injected into the mice followed by injection of fAuNPs (1 mg ml^{-1} , $100 \mu\text{l}$), and the tumors were irradiated under 808-nm laser (1 W cm^{-2} , 10 min) at 12 hours after injection of fAuNPs.

The vascular perfusion was assessed by intravenous injection with FITC-lectin (1 mg ml^{-1} , $100 \mu\text{l}$). Ten minutes after the injection, mice were sacrificed and tumors were collected. The tumor sections were stained with anti-CD31 antibody for the blood vessels (red) and DAPI for the cell nucleus (blue). The perfusion area was estimated by calculating lectin⁺ area (green) in a percent per CD31⁺ area (red).

Micro-CT imaging of tumor vessels

mice were sacrificed and perfused intracardiacally with silicone rubber radiopaque compound Microfil (CT contrast agent). Subsequently, the tumors were excised and preserved in 4% formalin. The tumor vessels were scanned with micro-CT imaging system.

Metabonomic analysis

Female BALB/c mice with CT26 tumors (1×10^6 CT26 cells per mouse) inoculated on their right flank were used for metabonomic analysis. When the tumor volume reached to $\sim 100 \text{ mm}^3$, the mice were treated with PBS or peTVD (three mice per group). After that, the tumors were collected and then stored at -80°C for later use.

Metabonomic analysis was carried out according to the previous work of our group. Briefly, 10 mg of collected tumor samples were mixed with 1 ml of extractant (acetonitrile:isopropanol:water = 3:3:2) followed by ultrasonic on ice bath for 1 min. Subsequently, the mixture was centrifuged ($1300g$, 5 min), and the supernate ($800 \mu\text{l}$) was mixed with Myristic acid-*d*27 (3 mg ml^{-1} , $20 \mu\text{l}$). Then, the mixture was blow-dried (N_2 environment) followed by addition of methoxyamine hydrochloride-pyridine (40 mg ml^{-1} , $20 \mu\text{l}$) at room temperature. Ninety minutes later, the resulting mixture was mixed with 1% trimethylchlorosilane in *N*-methyl-*N*-(trimethylsilyl) trifluoroacetamide ($90 \mu\text{l}$) and then coincubated at 37°C for 30 min. After centrifugation, the supernatant ($80 \mu\text{l}$) was collected for subsequent GC-MS analysis.

In vivo therapeutic effect

Female BALB/c mice with CT26 tumors (1×10^6 CT26 cells per mouse) inoculated on their right flank were used to assess the in vivo therapeutic effect. The mice were randomly divided into five groups (six mice per group). When the tumor volume reached to $\sim 100 \text{ mm}^3$, the mice were treated with PBS, fAuNPs with NIR, DMXAA, fAuNPs + DMXAA, and fAuNPs + DMXAA with NIR (peTVD) through tail vein injection, respectively. Tumor volumes and body weight were measured every 2 days during the treatment.

Comparison of peTVD with clinical therapies

Female BALB/c mice were xenografted with CT26 tumor by subcutaneous injection of luc-CT26 cells (1×10^6 cells per mouse) on their right flank. The mice were randomly divided into five groups (five mice per group). When the tumor volumes reached to $\sim 100 \text{ mm}^3$, the mice were treated with PBS, surgical resection, chemotherapy (DOX, 4 mg kg^{-1}), radiotherapy (8 gray), and peTVD, respectively. The tumor growth was monitored with the bioluminescence imaging every 7 days.

Platelet aggregation assay

Hemolysis assay

Blood samples were obtained from the heart of mice by using blood collection tube containing Na-heparin as an anticoagulant. Then, blood samples (100 μ l) were respectively added into PBS (900 μ l, as negative control), deionized water (900 μ l, as positive control), DMXAA (15 mg kg^{-1} , 900 μ l), and fAuNPs (1 mg ml^{-1} , 900 μ l). After coincubation in shaking incubator at 37°C for 4 hours, the mixtures were centrifuged (300g, 5 min) to remove unbroken red blood cell and the clots.

Subsequently, the supernate was added into a 96-well plate followed by measuring their absorbance at 540 nm. The data are presented as means \pm SD in triplicate.

Blood coagulation tests

To evaluate the blood compatibility of peTVD, blood coagulation indices were tested. Female BALB/c mice with CT26 tumors (1×10^6 CT26 cells per mouse) inoculated on their right flank were used for the blood routine examination and blood biochemistry analysis. The mice were randomly divided into three groups (three mice per group). When the tumor volumes reached to $\sim 100 \text{ mm}^3$, the mice were treated with PBS, fAuNPs, and peTVD via intravenous administration, respectively. The blood samples were collected from the heart and added to the anticoagulant tube. The sample was then centrifuged at 3000 rpm for 15 min to separate the plasma. The blood coagulation indices (including APTT, PT, fibrinogen-FIB, and TT) were tested.

Blood routine examination and blood biochemistry analysis

To evaluate the blood compatibility of peTVD, blood biochemical indexes and blood routine indexes were tested. Female BALB/c mice with CT26 tumors (1×10^6 CT26 cells per mouse) inoculated on their right flank were used for the blood routine examination and blood biochemistry analysis. The mice were randomly divided into three groups (three mice per group). When the tumor volume reached to $\sim 100 \text{ mm}^3$, the mice were treated with PBS, fAuNPs, and peTVD via intravenous administration, respectively. Seven days after administration, blood samples were collected from the heart (100 μ l each mouse). The blood routine examination was carried out by Auto Hematology Analyzer (MC-6200VET), and blood biochemistry analysis was performed by biochemical auto analyzer (MNCHIP, Tianjin, China).

Statistical analysis and sample collection

Significance among more than two groups was calculated using analysis of variance (ANOVA) Tukey's test by using SPSS 22.0. For cell experiments and in vivo experiments, investigators performing operations were blinded to treatment groups. In in vivo experiments, animals were randomly divided into different groups.

Download a pre-proof for this paper from bioRxiv preprint.

This is an open-access article distributed under the terms of the [Creative Commons Attribution-NonCommercial license](#), which permits use, distribution, and reproduction in any medium, so long as the resultant use is **not** for commercial advantage and provided the original work is properly cited.

REFERENCES AND NOTES

1. ↪ L. B. Rivera, G. Bergers, Tumor angiogenesis, from foe to friend. *Science* **349**, 694–695 (2015).
[Abstract/FREE Full Text](#) [Google Scholar](#)
2. R. S. Kerbel, Tumor angiogenesis. *N. Engl. J. Med.* **358**, 2039–2049 (2008). [CrossRef](#) [PubMed](#) [Web of Science](#)
[Google Scholar](#)
3. ↪ S. M. Weis, D. A. Cheresh, Tumor angiogenesis: Molecular pathways and therapeutic targets. *Nat. Med.* **17**, 1359–1370 (2011). [CrossRef](#) [PubMed](#) [Google Scholar](#)
4. ↪ J. Sawada, T. Urakami, F. Li, A. Urakami, W. Zhu, M. Fukuda, D. Y. Li, E. Ruoslahti, M. Komatsu, Small GTPase R-Ras regulates integrity and functionality of tumor blood vessels. *Cancer Cell* **22**, 235–249 (2012). [CrossRef](#) [PubMed](#) [Web of Science](#) [Google Scholar](#)
5. ↪ M. Gil, M. Seshadri, M. P. Komorowski, S. I. Abrams, D. Kozbor, Targeting CXCL12/CXCR4 signaling with oncolytic virotherapy disrupts tumor vasculature and inhibits breast cancer metastases. *Proc. Natl. Acad. Sci. U.S.A.* **110**, E1291–E1230 (2013). [Abstract/FREE Full Text](#) [Google Scholar](#)
6. ↪ Z. Zhen, W. Tang, Y.-J. Chuang, T. Todd, W. Zhang, X. Lin, G. Niu, G. Liu, L. Wang, Z. Pan, X. Chen, J. Xie, Tumor vasculature targeted photodynamic therapy for enhanced delivery of nanoparticles. *ACS Nano* **8**, 6004–6013 (2014). [CrossRef](#) [PubMed](#) [Google Scholar](#)
7. ↪ P. Hinnen, F. A. L. M. Eskens, Vascular disrupting agents in clinical development. *Br. J. Cancer* **96**, 1159–1165 (2007). [CrossRef](#) [PubMed](#) [Google Scholar](#)
8. ↪ M. Zhang, J.-J. Ye, Y. Xia, Z.-Y. Wang, C.-X. Li, X.-S. Wang, W. Yu, W. Song, J. Feng, X.-Z. Zhang, Platelet-mimicking biotaxis targeting vasculature-disrupted tumors for cascade amplification of hypoxia-sensitive therapy. *ACS Nano* **13**, 14230–14240 (2019). [Google Scholar](#)
9. ↪ W. Song, Z. Tang, D. Zhang, M. Li, J. Gu, X. Chen, A cooperative polymeric platform for tumor-targeted drug delivery. *Chem. Sci.* **7**, 728–736 (2016). [Google Scholar](#)
10. ↪ R. L. Stone, A. K. Sood, R. L. Coleman, Collateral damage: Toxic effects of targeted antiangiogenic therapies in ovarian cancer. *Lancet Oncol.* **11**, 465–475 (2010). [CrossRef](#) [PubMed](#) [Web of Science](#)
[Google Scholar](#)

PDF

Help

eaax2693 (2019). [Abstract/FREE Full Text](#) [Google Scholar](#)

13. [↵](#) W.-H. Chen, G.-F. Luo, Q. Lei, S. Hong, W.-X. Qiu, L.-H. Liu, S.-X. Cheng, X.-Z. Zhang, Overcoming the heat endurance of tumor cells by interfering with the anaerobic glycolysis metabolism for improved photothermal therapy. *ACS Nano* **11**, 1419–1431 (2017). [Google Scholar](#)
14. Q. Lei, S.-B. Wang, J.-J. Hu, Y.-X. Lin, C.-H. Zhu, L. Rong, X.-Z. Zhang, Stimuli-responsive “cluster bomb” for programmed tumor therapy. *ACS Nano* **11**, 7201–7214 (2017). [Google Scholar](#)
15. D.-W. Zheng, S. Hong, L. Xu, C.-X. Li, K. Li, S.-X. Cheng, X.-Z. Zhang, Hierarchical micro-/nanostructures from human hair for biomedical applications. *Adv. Mater.* **30**, 1800836 (2018). [Google Scholar](#)
16. [↵](#) W. Tang, Z. Dong, R. Zhang, X. Yi, K. Yang, M. Jin, C. Yuan, Z. Xiao, Z. Liu, L. Cheng, Multifunctional two-dimensional core–shell MXene@Gold nanocomposites for enhanced photo–radio combined therapy in the second biological window. *ACS Nano* **13**, 284–294 (2019). [Google Scholar](#)
17. [↵](#) D. Zhang, T. Wu, X. Qin, Q. Qiao, L. Shang, Q. Song, C. Yang, Z. Zhang, Intracellularly generated immunological gold nanoparticles for combinatorial photothermal therapy and immunotherapy against tumor. *Nano Lett.* **19**, 6635–6646 (2019). [Google Scholar](#)
18. R. Jin, Z. Liu, Y. Bai, Y. Zhou, J. J. Gooding, X. Chen, Core–satellite mesoporous silica–gold nanotheranostics for biological stimuli triggered multimodal cancer therapy. *Adv. Funct. Mater.* **28**, 1801961 (2018). [Google Scholar](#)
19. [↵](#) P. Wang, L. Zhang, W. Zheng, L. Cong, Z. Guo, Y. Xie, L. Wang, R. Tang, Q. Feng, Y. Hamada, K. Gonda, Z. Hu, X. Wu, X. Jiang, Thermo-triggered release of CRISPR-Cas9 system by lipid-encapsulated gold nanoparticles for tumor therapy. *Angew. Chem. Int. Ed.* **57**, 1491–1496 (2018). [Google Scholar](#)
20. [↵](#) K. Jiang, D. A. Smith, A. Pinchuk, Size-dependent photothermal conversion efficiencies of plasmon-heated gold nanoparticles. *J. Phys. Chem. C* **117**, 27073–27080 (2013). [Google Scholar](#)
21. [↵](#) C. Liu, Z. Gao, J. Zeng, Y. Hou, F. Fang, Y. Li, R. Qiao, L. Shen, H. Lei, W. Yang, M. Gao, Magnetic/upconversion fluorescent NaGdF₄:Yb,Er nanoparticle-based dual-modal molecular probes for imaging tiny tumors in vivo. *ACS Nano* **7**, 7227–7240 (2013). [Google Scholar](#)
22. [↵](#) G. González-Rubio, A. Guerrero-Martínez, L. M. Liz-Marzán, Reshaping, fragmentation, and assembly of gold nanoparticles assisted by pulse lasers. *Acc. Chem. Res.* **49**, 678–686 (2016). [CrossRef](#) [PubMed](#) [Google Scholar](#)
23. [↵](#) J. Wei, K. Niikura, T. Higuchi, T. Kimura, H. Mitomo, H. Jinnai, Y. Joti, Y. Bessho, Y. Nishino, Y. Matsuo, K. Ijiri, Yolk/Shell assembly of gold nanoparticles by size segregation in solution. *J. Am. Chem. Soc.* **138**, 3274–3277 (2016). [Google Scholar](#)

PDF

Help

[Google Scholar](#)

26. ↪ D. Liu, W. Chen, K. Sun, K. Deng, W. Zhang, Z. Wang, X. Jiang, Resettable, multi-readout logic gates based on controllably reversible aggregation of gold nanoparticles. *Angew. Chem. Int. Ed.* **50**, 4103–4107 (2011). [PubMed](#) [Google Scholar](#)
27. ↪ T. Kim, N. Lee, D. R. Arifin, I. Shats, M. Janowski, P. Walczak, T. Hyeon, J. W. M. Bulte, In vivo micro-CT imaging of human mesenchymal stem cells labeled with gold-poly-L-lysine nanocomplexes. *Adv. Funct. Mater.* **27**, 1604213 (2017). [Google Scholar](#)
28. ↪ G. M. Tozer, C. Kanthou, B. C. Baguley, Disrupting tumour blood vessels. *Nat. Rev. Cancer* **5**, 423–435 (2005). [CrossRef](#) [PubMed](#) [Web of Science](#) [Google Scholar](#)
29. ↪ C. Kim, H. Yang, Y. Fukushima, P. E. Saw, J. Lee, J.-S. Park, I. Park, J. Jung, H. Kataoka, D. Lee, W. D. Heo, I. Kim, S. Jon, R. H. Adams, S.-I. Nishikawa, A. Uemura, G. Y. Koh, Vascular RhoJ is an effective and selective target for tumor angiogenesis and vascular disruption. *Cancer Cell* **25**, 102–117 (2014). [CrossRef](#) [PubMed](#) [Google Scholar](#)
30. ↪ S. Li, Q. Jiang, S. Liu, Y. Zhang, Y. Tian, C. Song, J. Wang, Y. Zou, G. J. Anderson, J.-Y. Han, Y. Chang, Y. Liu, C. Zhang, L. Chen, G. Zhou, G. Nie, H. Yan, B. Ding, Y. Zhao, A DNA nanorobot functions as a cancer therapeutic in response to a molecular trigger in vivo. *Nat. Biotechnol.* **36**, 258–264 (2018). [CrossRef](#) [PubMed](#) [Google Scholar](#)
31. ↪ S. Li, Y. Zhang, J. Wang, Y. Zhao, T. Ji, X. Zhao, Y. Ding, X. Zhao, R. Zhao, F. Li, X. Yang, S. Liu, Z. Liu, J. Lai, A. K. Whittaker, G. J. Anderson, J. Wei, G. Nie, Nanoparticle-mediated local depletion of tumour-associated platelets disrupts vascular barriers and augments drug accumulation in tumours. *Nat. Biomed. Eng.* **1**, 667–679 (2017). [Google Scholar](#)
32. ↪ C. Zhang, L. Zhang, W. Wu, F. Gao, R.-Q. Li, W. Song, Z.-N. Zhuang, C.-J. Liu, X.-Z. Zhang, Artificial super neutrophils for inflammation targeting and HClO generation against tumors and infections. *Adv. Mater.* **31**, e1901179 (2019). [Google Scholar](#)
33. ↪ R. L. Siegel, K. D. Miller, A. Jemal, Cancer statistics, 2019. *CA Cancer J. Clin.* **69**, 7–34 (2019). [CrossRef](#) [PubMed](#) [Google Scholar](#)
34. ↪ S. Hassan, G. Prakash, A. Bal Ozturk, S. Saghadzadeh, M. Farhan Sohail, J. Seo, M. Remzi Dokmeci, Y. S. Zhang, A. Khademhosseini, Evolution and clinical translation of drug delivery nanomaterials. *Nano Today* **15**, 91–106 (2017). [Google Scholar](#)
35. ↪ D. Ben-David, S. Srouji, K. Shapira-Schweitzer, O. Kossover, E. Ivanir, G. Kuhn, R. Müller, D. Seliktar, E. Livne, Low dose BMP-2 treatment for bone repair using a PEGylated fibrinogen hydrogel matrix. *Biomaterials* **34**, 2902–2910 (2013). [CrossRef](#) [PubMed](#) [Google Scholar](#)

PDF

Help

the data. S.H. and D.-W.Z. performed in vivo experiments. S.H., D.-W.Z., C.Z., S.-X.C., and X.-Z.Z. cowrote the manuscript. All authors discussed the results and reviewed the manuscript. **Competing interests:** The authors declare that they have no competing interests. **Data and materials availability:** All data needed to evaluate the conclusions in the paper are present in the paper and/or the Supplementary Materials. Additional data related to this paper may be requested from the authors.

Copyright © 2020 The Authors, some rights reserved; exclusive licensee American Association for the Advancement of Science. No claim to original U.S. Government Works. Distributed under a Creative Commons Attribution NonCommercial License 4.0 (CC BY-NC).

View Abstract

Recommended articles from TrendMD

Gold photothermal therapy: A positive for negative margins

Miles A. Miller, *Sci Transl Med*, 2018

COX-2 inhibition potentiates antiangiogenic cancer therapy and prevents metastasis in preclinical models.

Lihong Xu et al., *Sci Transl Med*, 2014

Nuclear phospho-Akt increase predicts synergy of PI3K inhibition and doxorubicin in breast and ovarian cancer.

Jeffrey J Wallin et al., *Sci Transl Med*, 2010

Loss of SPDEF and gain of TGFBI activity after androgen deprivation therapy promote EMT and bone metastasis of prostate cancer

Wei-Yu Chen et al., *Sci Signal*, 2017

Engineering nanoparticles to locally activate T cells in the tumor microenvironment

Dangge Wang et al., *Sci Immunol*, 2019

LyP-1 peptide-functionalized gold nanoprisms for SERRS imaging and tumor growth suppressing by PTT induced-hyperthermia

Huang et al., *Chinese Chemical Letters*, 2019

Immune-adjuvant loaded Bi₂Se₃ nanocage for photothermal-improved PD-L1 checkpoint blockade immune-tumor metastasis therapy

Yilin Song et al., *Nano Research*, 2019

Theranostic nanoparticles with tumor-specific enzyme-triggered size reduction and drug release to perform photothermal therapy for breast cancer treatment

Liu et al., *Acta Pharmaceutica Sinica B*, 2019

NIR light-induced tumor phototherapy using ICG delivery system based on platelet-membrane-camouflaged hollow bismuth selenide nanoparticles

Ding et al., *Chinese Chemical Letters*, 2019

Biomimetic albumin-modified gold nanorods for photothermo-chemotherapy and macrophage polarization modulation

Li et al., *Acta Pharmaceutica Sinica B*, 2018

PDF

Help



Table of Contents

View this article with *LENS*

ARTICLE TOOLS

 Email

 Print

 Request permissions

 Share

 Download Powerpoint

 Alerts

 Citation tools

MY SAVED FOLDERS

 Save to my folders

STAY CONNECTED TO SCIENCE ADVANCES

- Facebook
- Twitter

SIMILAR ARTICLES IN:

- Google Scholar

PDF

Help



ECOLOGY

Blue carbon from the past forecasts the future

WORKING LIFE

No place like home

[Table of Contents](#)

About Us

- [Journals](#)
- [News from Science](#)
- [Leadership](#)
- [Team Members](#)
- [Work at AAAS](#)

For Advertisers

- [Advertising Kit](#)
- [Awards and Prizes](#)
- [Custom Publishing](#)
- [Webinars](#)

For Authors

- [Submit](#)
- [Information for Authors](#)
- [Editorial Policies](#)

For Librarians

- [Manage Your Institutional Subscription](#)
- [Information for Librarians](#)
- [Request a Quote](#)
- [FAQs](#)

Related Sites

- [AAAS.org](#)
- [EurekAlert!](#)
- [Science in the Classroom](#)
- [Science Magazine Japanese](#)

Help

PDF

Help

Dalhousie University

College of Pharmacy, Dalhousie University
Halifax, Nova Scotia, Canada

Scientist II - Computational Biologist


Myriad Genetics, Inc
South San Francisco, California

Faculty Positions in the Department of Electrical and Electronic Engineering

Southern University of Science and Technology (SUSTech)
Shenzhen, China

[MORE JOBS ►](#)

NAVIGATE THIS ARTICLE

- Article
 - Abstract
 - INTRODUCTION
 - RESULTS
 - DISCUSSION
 - MATERIALS AND METHODS
 - SUPPLEMENTARY MATERIALS
 - REFERENCES AND NOTES
- Figures & Data
- Info & Metrics
- eLetters
-  PDF

PDF

Help

Read the Latest Issue of *Science*

5 June 2020

Vol 368, Issue 6495

FEATURE

Double trouble

SOCIAL SCIENCE: COVID-19

Which interventions work best in a pandemic?

ECOLOGY

Stay Connected



© 2020 American Association for the Advancement of Science. All rights reserved. AAAS is a partner of HINARI, AGORA, OARE, CHORUS, CLOCKSS, CrossRef and COUNTER. *Science Advances* ISSN 2375-2548.

[Terms of Service](#)

[Privacy Policy](#)

[Contact AAAS](#)

PDF

Help